Chinese Journal of Aeronautics, (2014),27(5): 1327–1333

Chinese Society of Aeronautics and Astronautics
& Beihang University

Chinese Journal of Aeronautics

cja@buaa.edu.cn
www.sciencedirect.com

SCC investigation of low alloy ultra-high strength steel 30CrMnSiNi2A in 3.5wt% NaCl solution by slow strain rate technique

Liu Jianhua *, **Guo Qiang, Yu Mei, Li Songmei**

Key Laboratory of Aerospace Materials & Performance (Ministry of Education), School of Materials Science and Engineering, Beihang University, Beijing 100191, China

Received 6 November 2013; revised 12 December 2013; accepted 12 February 2014
Available online 15 March 2014

KEYWORDS

Hydrogen;
NaCl solution;
Stress corrosion cracking;
Slow strain rate technique;
Ultra-high strength steel

Abstract To evaluate stress corrosion cracking (SCC) mechanism of low alloy ultra-high strength steel 30CrMnSiNi2A in environment containing NaCl, SCC behavior of the steel in 3.5wt% NaCl solution is investigated by slow strain rate technique (SSRT) with various strain rates and applied potentials, surface analysis technique, and electrochemical measurements. SCC susceptibility of the steel increases rapidly with strain rate decreasing from 1×10^{-5} s^{-1} to 5×10^{-7} s^{-1}, and becomes stable when strain rate is lower than 5×10^{-7} s^{-1}. SCC propagation of the steel in the solution at open circuit potential (OCP) needs sufficient hydrogen which is supplied at a certain strain rate. Fracture surface at OCP has similar characteristics with that at cathodic polarization -1000 mV_{SCE}, which presents characteristic fractography of hydrogen induced cracking (HIC). All of these indicate that SCC behavior of the steel in the solution at OCP is mainly controlled by HIC rather than anodic dissolution (AD).

1. Introduction

It is widely acknowledged that SCC is a phenomenon associated with conjoint electrochem-mechanical effect.[1] Stress corrosion cracking usually initiates unexpectedly when a susceptible material with subcritical stress is subjected in an aggressive environment, and it usually results in sudden and catastrophic accidence.[2–6] SCC behavior of ultra-high strength steel (UHSS) has attracted extensive attention for its extremely significant service safety and SCC behavior of high strength steel has been investigated for decades. The SCC mechanisms of high strength steel are widely accepted as two categories, including AD and HIC.[7]

Oehlert and Atrens[8] found that SCC propagation of AerMet100 at OCP in netrural NaCl solution was mainly controlled by HIC. On the contrary, Wu et al.[9] found that AD controlled SCC behavior of AerMet100 at OCP in acidic chloride solution. Liu et al.[10] reported that AerMet100 showed better anti-SCC properties than 300M did. Figueroa and Robinson[11,12] suggested that AerMet100 was more resistant to

* Corresponding author. Tel.: +86 10 82317103.
E-mail addresses: liujh@buaa.edu.cn (J. Liu), guoqiang832003@163.com (Q. Guo).

Peer review under responsibility of Editorial Committee of CJA.

ELSEVIER Production and hosting by Elsevier

http://dx.doi.org/10.1016/j.cja.2014.03.025

hydrogen embrittlement than 300M due to reverted austenite surrounding the martensite laths, which prevented hydrogen from being absorbed in more susceptible martensite phase. Graça et al.[13] found that SCC propagation of 300M steel was caused by hydrogen absorbed around pits. Ramamurthy et al.[14,15] supposed that the stress corrosion cracking velocity was dependent on the applied stress rate and the crack tip strain rate, independent from composition of steels AISI 4340 and 3.5NiCrMoV. Fang et al.[16] suggested that SCC only occurred when the local strain rate was smaller than the upper susceptible local strain rate for SCC.

30CrMnSiNi2A is a kind of low-alloyed martensite UHSS with remarkable application in aviation, aerospace, automobile, and chemical industries, etc., such as landing gear, rocket shell, high-strength bolt and so on. Zhu and Zhai[17] investigated stress corrosion cracking of 30CrMnSiNi2A using double cantilever beam (DCB) specimens and found that SCC was controlled by HIC at cathodic polarization and by AD at anodic polarization, respectively, but it was not sure that SCC at OCP was controlled by HIC or combination of HIC and AD. Zhu and Yang[18] suggested that hydrogen often caused embrittlement of 30CrMnSiNi2A and inhibited plastic deformation. Chu et al.[19,20] investigated low alloy high strength steels with different strength levels in deionized water or aqueous solution with H_2S using wedge opening load (WOL) methods and found that K_{ISCC} increased and the da/dt decreased with strength increasing in all the environments.

In the present investigation, SCC behavior of low alloy UHSS 30CrMnSiNi2A in neutral 3.5wt% NaCl solution is investigated by SSRT with different strain rates and polarization potentials, electrochemical measurements and surface analysis technique. The effect of strain rate on SCC behavior is analyzed and SCC mechanisms at OCP, cathodic and anodic polarization potentials are discussed in detail.

2. Experimental

2.1. Materials

The predominant chemical composition of low alloy ultra-high strength steel 30CrMnSiNi2A is listed in Table 1. Its heat treatment is shown as follows: air heat treatment at (890 ± 10) °C for 1 h, subsequently quenched in oil; tempered at (280 ± 5) °C for 2–3 h, air cooling to ambient temperature. The microstructure of the steel mainly consists of martensite lath, with a small amount of bainite and retained austenite.[21] The yield strength $\sigma_{0.2}$ and tensile strength σ_b of 30CrMnSiNi2A are 1425 MPa and 1800 MPa, respectively. The tensile specimens were machined into smooth flat-plate specimens, as shown in Fig. 1, according to aviation industry standard of China HB5254. The length of the gauge section is 20 mm. Prior to each SCC test, the gauge section of tensile specimens was polished in the longitudinal direction by successive silicon carbide paper up to 1000#, then rinsed with deionized water, degreased in dehydrated ethanol and acetone by ultrasonic sound, and then dried in air. Epoxy resin was applied on the surface of the specimens except for the gauge sections.

Table 1 Predominant chemical composition of 30CrMnSiNi2A.

Element	C	Si	Cr	Mn	Ni	Fe
wt%	0.27	1.0	1.10	1.20	1.60	Bal.

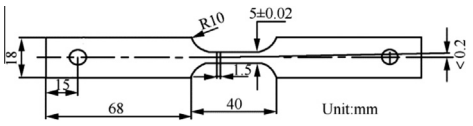

Fig. 1 Schematic diagram of flat-plate tensile specimens used in this paper.

2.2. SSRT

SSRT was carried out according to ASTM G129-00(2006).[22] Different strain rates ($\dot{\varepsilon}$) ranging from $1\times10^{-4}\,s^{-1}$ to $1.67\times10^{-7}\,s^{-1}$ were conducted on the tensile specimens at OCP in 3.5wt% NaCl solution at 35 °C. Polarization potentials (E) of $-1000\,mV_{SCE}$ and $-500\,mV_{SCE}$ were applied on the specimens at a strain rate of $5\times10^{-7}\,s^{-1}$ in the solution at 35 °C, with electric power supplied by a PAR263A potentiostat/galvanostat instrument (Ametek, USA). Prior to SSRT test, the pre-loading force was conducted at about 100 N to avoid the gap between two gears of a SSRT machine (Letry Co. Ltd., Xi'an, China).

2.3. Electrochemical measurements

An electrochemical working station (VersaSTAT MC-4, Ametek, USA) was employed to carry out electrochemical measurements using a traditional 3-electrode cell, with the steel as a working electrode, a large area of Pt plate (20 mm × 50 mm) as a counter electrode, and KCl saturated calomel electrode (SCE) as a reference electrode. Potentiodynamic polarization measurement is carried out on the steel with potential sweep rates ($\dot{E}$) of 0.5 mV/s and 50 mV/s in a potential ranging from −500 mV (vs OCP) to −200 mV (vs SCE). The solution for electrochemical measurements is 3.5wt% NaCl aqueous solution at room temperature (25 °C ± 1 °C).

2.4. Surface characterization

Corrosion product in the fracture was cleared by mixture of HCl and distilled water (1:1 in volume) with a small amount of hexamethylenetetramine by ultrasound for 3 min. Surface morphologies of the fracture and its side were observed by Field Emission Scanning Electron Microscope (FE-SEM, Apollo300, CamScan, UK).

3. Results

3.1. Strain rates

Fig. 2 shows stress–strain curves with various strain rates of the steel at OCP in 3.5wt% NaCl solution. With strain rates decreasing from $1\times10^{-4}\,s^{-1}$ to $1.67\times10^{-7}\,s^{-1}$, tensile strength and strain to fracture decrease remarkably; especially for strain to fracture between $1\times10^{-6}\,s^{-1}$ and $5\times10^{-7}\,s^{-1}$, which shows great difference. However, it has little difference between $5\times10^{-7}\,s^{-1}$ and $1.67\times10^{-7}\,s^{-1}$.

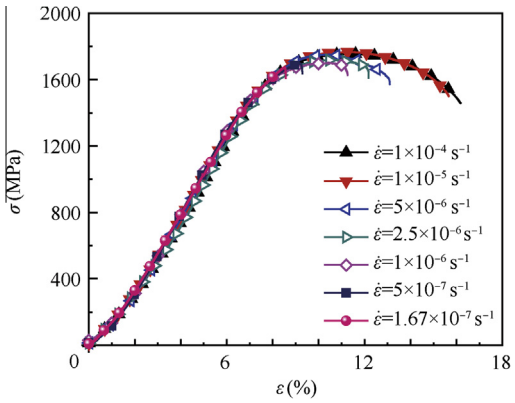

Fig. 2 Stress–strain curves of steel with various strain rates in 3.5wt% NaCl solution at OCP.

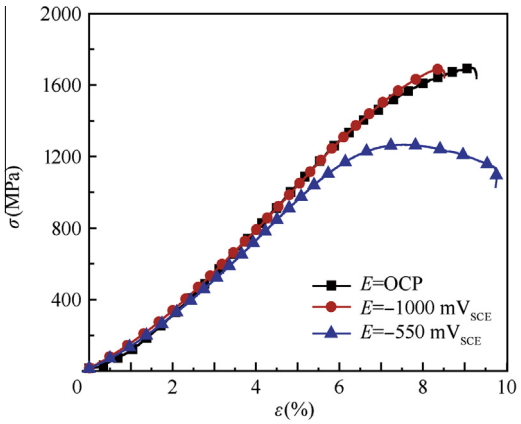

Fig. 4 Stress–strain curves of steel under various potentials at $\dot{\varepsilon} = 5 \times 10^{-7}\ s^{-1}$ in 3.5wt% NaCl solution.

Fig. 3(a) and (b) shows the ratios of reduction-in-area (Ψ) and elongation (δ) at different strain rates. It could be found that Ψ and δ at OCP decrease remarkably with strain rate decreasing. The curves should be divided into three regions according to Ψ and δ variation with different strain rates. Ψ and δ show small variation in strain rate range from $1 \times 10^{-4}\ s^{-1}$ to $1 \times 10^{-5}\ s^{-1}$, great amplitude from $1 \times 10^{-5}\ s^{-1}$ to $5 \times 10^{-7}\ s^{-1}$, and nearly unchanged from $5 \times 10^{-7}\ s^{-1}$ to $1.67 \times 10^{-7}\ s^{-1}$. According to Eq. (1), SCC susceptibility was evaluated by the loss of reduction-in-area (I_Ψ) and elongation (I_δ), which is inversely proportional to Ψ and δ. It indicates that the steel shows different SCC susceptibility at different strain rates. SCC susceptibility increases very rapidly with strain rate decreasing from $1 \times 10^{-5}\ s^{-1}$ to $5 \times 10^{-7}\ s^{-1}$. In the strain rate range below $5 \times 10^{-7}\ s^{-1}$, it shows similar SCC susceptibility independent from strain rate.

$$\begin{cases} I_\delta = \dfrac{\delta_{air} - \delta_{sol}}{\delta_{air}} \times 100\% \\ I_\psi = \dfrac{\psi_{air} - \psi_{sol}}{\psi_{air}} \times 100\% \end{cases} \quad (1)$$

where δ_{air} and Ψ_{air} are percentages of elongation and reduction-in-area in air, respectively, and δ_{sol} and Ψ_{sol} are percentages of elongation and reduction-in-area in 3.5wt% NaCl solution, respectively.

3.2. Applied potentials

Fig. 4 shows stress–strain curves of the steel under different applied potentials at a strain rate of $5 \times 10^{-7}\ s^{-1}$. It could be found that stress–strain curve at E = OCP gets close to that at $E = -1000\ mV_{SCE}$. But stress–strain curve at $-500\ mV_{SCE}$ shows much difference with the others. The stress–strain curve at $E = -500\ mV_{SCE}$ shows lower yield and fracture strength and longer strain than the others. The fracture time and strain at $-500\ mV_{SCE}$ is more than those at $-1000\ mV_{SCE}$ and OCP.

Table 2 displays percentage of Ψ and δ at $5 \times 10^{-7}\ s^{-1}$ under different applied potentials, such as $-1000\ mV_{SCE}$, $-500\ mV_{SCE}$ and OCP. Percentages of Ψ and δ at $-1000\ mV_{SCE}$ are close to that at OCP. Ψ and δ at $-500\ mV_{SCE}$ are much higher than those at $-1000\ mV_{SCE}$ and OCP; high value of Ψ is mostly due to

Table 2 Reduction-in-area and elongation ratios of steel under various potentials at $\dot{\varepsilon} = 5 \times 10^{-7}\ s^{-1}$ in 3.5wt% NaCl solution.

Parameters	E = OCP	$E = -500\ mV_{SCE}$	$E = -1000\ mV_{SCE}$
δ (%)	2.50	5.80	2.30
Ψ (%)	4.5	32.93	2.27

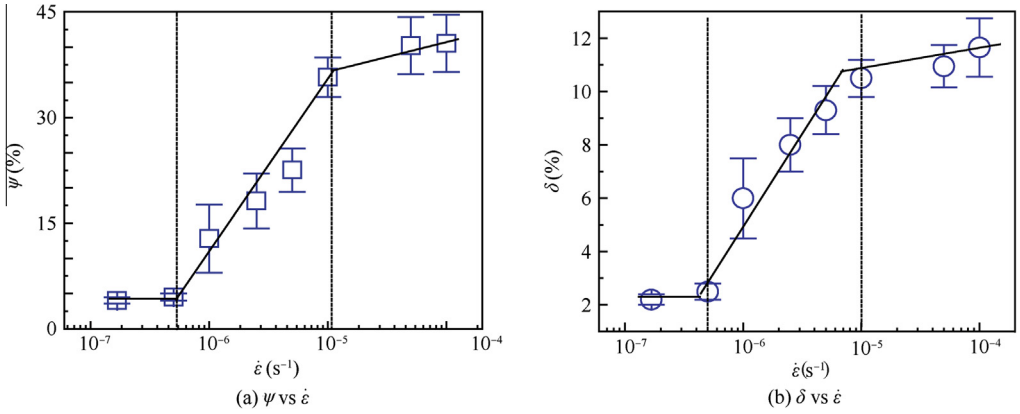

Fig. 3 Reduction-in-area and elongation ratios of steel with different strain rates in 3.5wt% NaCl solution at OCP.

seriously anodic dissolution, and the value of δ at $-500\ mV_{SCE}$ indicates that ductile tensile properties of the steel at $-500\ mV_{SCE}$ are much better than those at OCP and $-1000\ mV_{SCE}$.

3.3. Fracture appearance

Fig. 5(a)–(f) shows SEM micrographs of fracture surface morphology of the steel tensile at various strain rates of $1\times10^{-5}\ s^{-1}$, $5\times10^{-6}\ s^{-1}$, $2.5\times10^{-6}\ s^{-1}$, $1\times10^{-6}\ s^{-1}$, $5\times10^{-7}\ s^{-1}$, and $1.67\times10^{-7}\ s^{-1}$ at OCP. Fig. 5(a) shows the main ductile fracture at $1\times10^{-5}\ s^{-1}$. The fracture presents deep dimple, which indicates that the steel has good toughness and little SCC characteristics. At $5\times10^{-6}\ s^{-1}$, the fracture surface is composed of a small quantity of secondary cracks with the other regions of plasticity (Fig. 5(b)); it indicates that the fracture has few SCC characteristics at $5\times10^{-6}\ s^{-1}$. There are mixed mode of transgranular, intergranular fracture and secondary cracks in a small region at $2.5\times10^{-5}\ s^{-1}$ (Fig. 5(c)). At $1\times10^{-6}\ s^{-1}$, fracture morphology is composed of intergranular fracture and secondary cracks in a small region, as shown in Fig. 5(d). At $5\times10^{-7}\ s^{-1}$ and $1.67\times10^{-7}\ s^{-1}$, it shows the same brittle fracture morphology, which is mainly composed of intergranular fracture and secondary cracks, as shown in Fig. 5(e) and (f), respectively. From Fig. 5(a)–(f), the fractography shows a rule of regular variation of SCC fracture from strain rate range from $2.5\times10^{-6}\ s^{-1}$ to $1.67\times10^{-7}\ s^{-1}$. The fractography indicates clear estimation of SCC susceptibility to successive strain rates, which coincides with the above-mentioned results of reduction-in-area and elongation obtained at different strain rates.

Fig. 6(a) and (b) shows fractography of the steel applied under $-1000\ mV_{SCE}$ and $-500\ mV_{SCE}$ at a strain rate of $5\times10^{-7}\ s^{-1}$, respectively. From macroscopic observation, the gauge section of the specimens at $-500\ mV_{SCE}$ was severely corroded, and the thickness was hardly reduced. The specimens at $-1000\ mV_{SCE}$ present metal luster without any corrosion, and show nearly no 'neck shrink'. Fractography at $-1000\ mV_{SCE}$ is composed of main intergranular fracture, secondary cracks and a small proportion of transgranular fracture. And fractography at $-500\ mV_{SCE}$ contains secondary cracks and intergranular fracture with obvious corrosion marks on the grains.

4. Discussions

4.1. SCC mechanism

Fig. 4 and Table 2 indicate that the specimen applied at potential $-500\ mV_{SCE}$ shows better ductile properties than the similar properties of the ones at $-1000\ mV_{SCE}$ and OCP. It illuminates

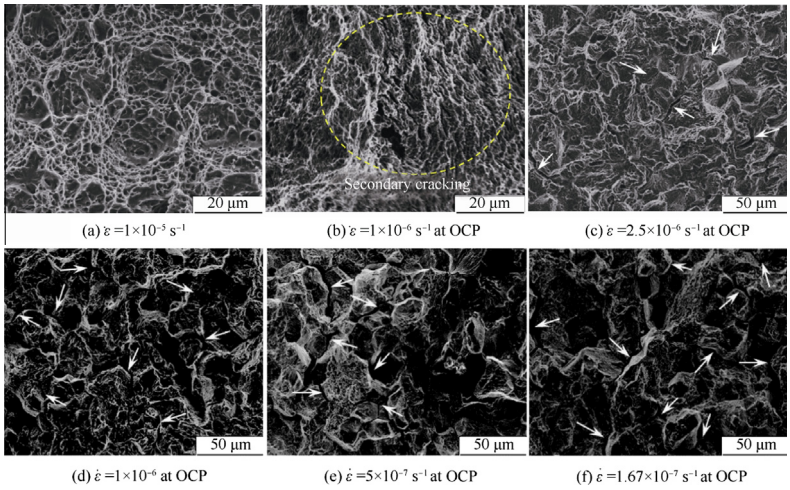

Fig. 5 SEM fractography of steel with different strain rates at OCP in 3.5wt% NaCl solution (arrows detect to secondary cracks).

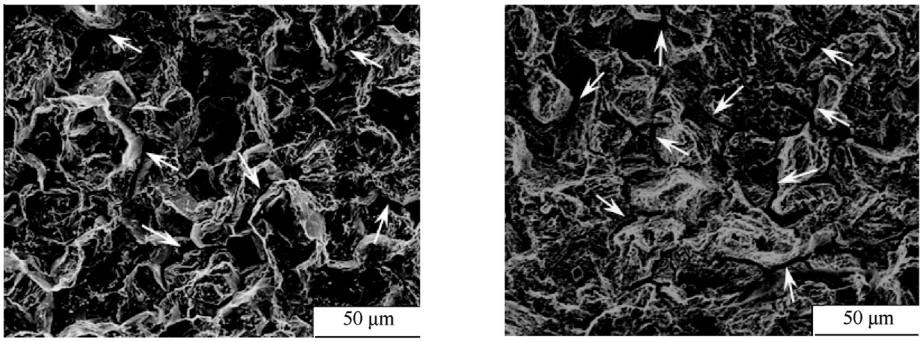

Fig. 6 SEM fractography of steel at $-1000\ mV_{SCE}$ and $-500\ mV_{SCE}$ with $\dot{\varepsilon}=5\times10^{-7}\ s^{-1}$ in 3.5wt% NaCl solution (arrows detect to secondary cracks).

that the fracture mechanism at $-500\ mV_{SCE}$ is different from the other two. The potentiodynamic polarization curves of the steel 30CrMnSiNi2A with slow and fast sweep rates in 3.5wt% NaCl solution are shown in Fig. 7. It shows that the corrosion potentials (E_{corr}) with sweep rates at 0.5 mV/s and 50 mV/s are about $-570\ mV_{SCE}$ and $-880\ mV_{SCE}$, respectively. According to previous works,[23–25] the potential range should be divided into three sections, which was controlled by different mechanisms. As polarization potentials was more than $-570mV_{SCE}$ ($E > -570\ mV_{SCE}$) and smaller than $-880\ mV_{SCE}$ ($E < -880\ mV_{SCE}$), SCC behavior of the steel is controlled by AD and HIC; SCC under potentials between $-570\ mV_{SCE}$ and $-880\ mV_{SCE}$ is due to the combined effect of the two mechanisms. That is to say, SCC behavior of the steel was under AD at $-500\ mV_{SCE}$, and HIC at $-1000\ mV_{SCE}$.

Fig. 8(a)–(c) shows typical intergranular fractography of the steel applied at $-1000\ mV_{SCE}$, OCP and $-500\ mV_{SCE}$ at a strain rate of $5\times10^{-7}\ s^{-1}$. Fig. 7(a) shows air cavity, paw pattern and tearing ridge on the clean grain facets of intergranular fracture at $-1000\ mV_{SCE}$. The characteristic fracture morphology shows an absolute HIC. In Figs. 6(a), (b) and 7(a), (c), it shows that the sizes of grain in the fracture at OCP are much bigger than that those at $-1000\ mV_{SCE}$, which indicates that hydrogen concentration at $-1000\ mV_{SCE}$ for hydrogen-induced cracking propagation is much more than that at OCP. Fig. 8(c) displays corroded grain and secondary cracks in the fracture at $-500\ mV_{SCE}$. SCC mechanism at $-500\ mV_{SCE}$ is confirmed to be mainly controlled by AD. From Fig. 8(c), fractography shows mainly intergranular and secondary cracks, with a certain cleavage fracture; grain facets in the fracture of tensile specimens at OCP display some air cavities, paw patterns, and tearing ridge. The identical characteristic fractography of tensile fracture at OCP and

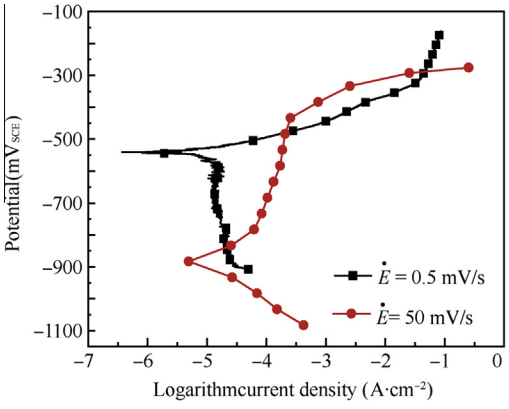

Fig. 7 Potentiodynamic polarization of the steel in 3.5wt% NaCl solution with sweep rates of 0.5 mV/s and 50 mV/s.

$-1000\ mV_{SCE}$ defines that HIC controls the mechanism during SCC propagation at both OCP and $-1000\ mV_{SCE}$.

4.2. Strain rate effect

The strain–stress curves, the values of Ψ and δ, and fractography at different strain rates indicate that stain rate has delicate effect on SCC behavior of the steel in 3.5wt% NaCl solution, which means that the steel shows remarkable SCC susceptibility to strain rates. In the high strain rate region, the fracture of the steel shows no or little SCC characteristic morphology, which mainly belongs to stress-dominated region. In the strain rate region from $1\times10^{-5}\ s^{-1}$ to $5\times10^{-7}\ s^{-1}$, the SCC susceptibility increases very remarkably with strain rate increasing, which is defined to be a SCC-dominated region. SCC susceptibility nearly unchanged in the region with strain rate below $5\times10^{-7}\ s^{-1}$. It indicates that with the strain rate below $5\times10^{-7}\ s^{-1}$, SCC susceptibility in the region is mainly dominated by electrochemical corrosion.

Fig. 9(a) and (c) shows the surface morphology of lateral side of the steel at $5\times10^{-7}\ s^{-1}$ and $1\times10^{-6}\ s^{-1}$, respectively. The morphology of lateral surface shows deep pits and long secondary cracks at $5\times10^{-7}\ s^{-1}$, and little pits and short secondary cracks at $1\times10^{-6}\ s^{-1}$, respectively. Fig. 9(b) and (d) shows fracture edge morphology of the steel tensile at $5\times10^{-7}\ s^{-1}$ and $1\times10^{-6}\ s^{-1}$, respectively. It shows that the diameter of the pits in the fracture at $5\times10^{-7}\ s^{-1}$ is up to 25 μm, the maximum depth of pits is more than 50 μm, and the secondary cracks are long and deep. On the contrary, pits in the fracture at $1\times10^{-6}\ s^{-1}$ are shallow and secondary cracks are smaller and shallower. It indicates that the steel was severely corroded under a synergistic effect with stress and electrochemical corrosion at a certain slow strain rate. It is consistent with the results of Figs. 2 and 3(a) and (b).

It is accepted that loading stress is not a sufficient but necessary factor for SCC behavior of UHSS, and other factors such as hydrogen concentration need to reach an appropriate value.[7] With strain rate decreasing, the tensile time to fracture increases. A certain strain rate has sufficient reaction time to reach a critical hydrogen concentration. Stress combined with critical hydrogen promotes the crack propagation. Therefore, hydrogen concentration produced by electrochemical corrosion increases with strain rate decreasing. In the strain rate range from $1\times10^{-5}\ s^{-1}$ to $5\times10^{-7}\ s^{-1}$, SCC susceptibility increases with hydrogen concentration increasing. When strain rate decreases to $5\times10^{-7}\ s^{-1}$ and $1.67\times10^{-7}\ s^{-1}$, the area of brittle region in the fracture, the fracture strength, and fracture strain change little, which means that strain rates below $5\times10^{-7}\ s^{-1}$ has a limited effect on SCC process. When hydrogen concentration increases to a certain content, SCC susceptibility becomes

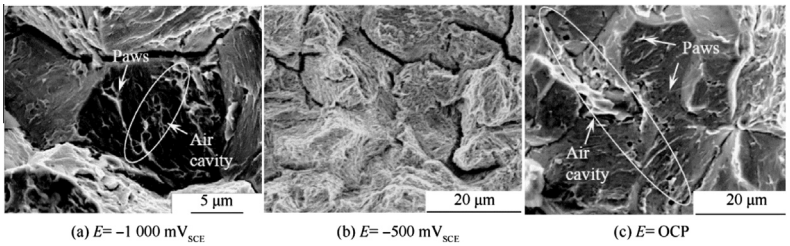

Fig. 8 SCC fracture morphology of steel at $\dot{\varepsilon} = 5\times10^{-7}\ s^{-1}$ in 3.5wt% NaCl solution under different potentials.

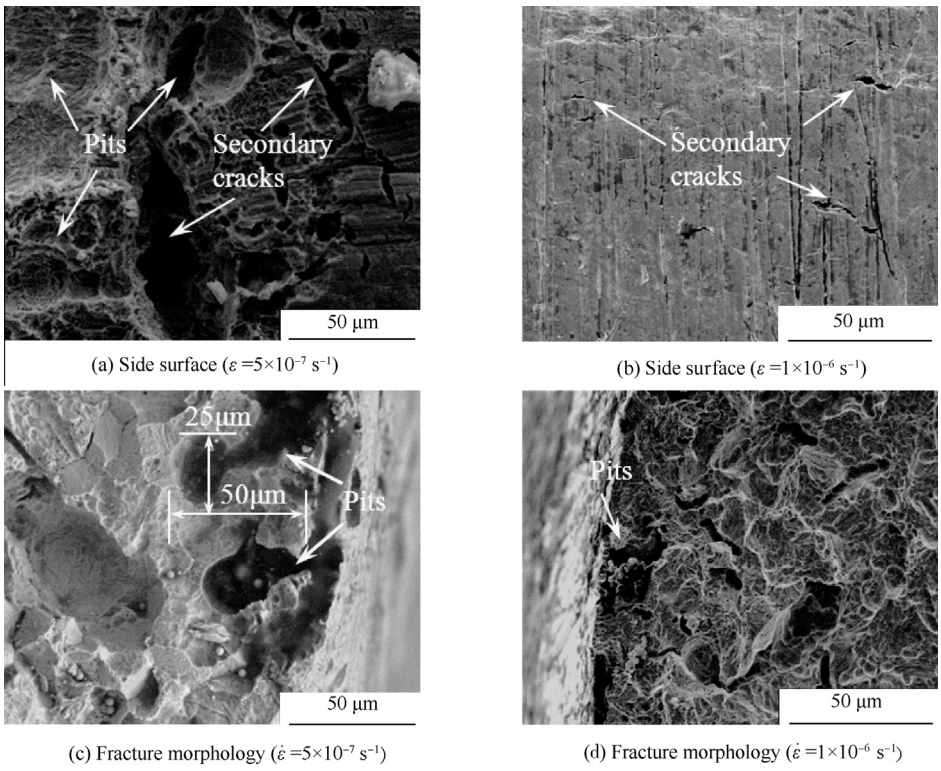

Fig. 9 Side surfaces and fracture morphology with strain rates $\dot{\varepsilon} = 5 \times 10^{-7}$ s^{-1} and 1×10^{-6} s^{-1} in 3.5wt% NaCl solution at OCP.

stable and the electrochemical corrosion dominates the SCC process. It indicates that the crack growth rate is between 1×10^{-6} s^{-1} and 5×10^{-7} s^{-1}.

5. Conclusions

(1) Stress corrosion cracking behavior of the steel 30CrMnSiNi2A shows obvious susceptibility to strain rate in 3.5wt% NaCl solution. SCC susceptibility increases with strain rate decreasing. In the range of strain rate from 1×10^{-5} s^{-1} to 5×10^{-7} s^{-1}, the steel shows more and more obvious SCC characteristics with strain rate decreasing, which is defined to be SCC-dominated. When strain rate is below 5×10^{-7} s^{-1}, SCC susceptibility becomes stable, which is mainly dominated by electrochemical corrosion.

(2) Hydrogen is a very important factor during SCC propagation of 30CrMnSiNi2A in 3.5wt% NaCl solution. SCC mechanism of 30CrMnSiNi2A at OCP and -1000 mV$_{SCE}$ is controlled by hydrogen induced cracking. However, SCC mechanism at -500 mV$_{SCE}$ is mainly due to anodic dissolution.

Acknowledgement

The authors acknowledge the financial support from the National Natural Science Foundation of China (No. 51171011).

References

1. Maeng WY, Lee HH, Kim UC. Environmental effects on the stress corrosion cracking susceptibility of 3.5NiCrMoV steels in high temperature water. *Corros Sci* 2005;**47**(8):1876–95.
2. Fang BY, Atrens A, Wang JQ, Han EH, Zhu ZY, Ke W. Review of stress corrosion cracking of pipeline steels in "Low" and "High" pH solutions. *J Mater Sci* 2003;**38**(1):127–32.
3. Liu C, Macdonald DD. Prediction of failures of low-pressure steam turbine disks. *J Press Vess Technol* 1997;**119**(4):393–400.
4. Hou WG, Zhang WF, Liu X, Wang ZR, Ding ML. Failure analysis of aviation torsional springs. *Chin J Aeronaut* 2011;**24**(4):527–32.
5. Winzer N, Atrens A, Song G, Ghali E, Dietzel W, Kainer KU, et al. A critical review of the stress corrosion cracking (SCC) of magnesium alloy. *Adv Eng Mater* 2005;**7**(8):659–93.
6. Yang B. Blade containment evaluation of civil aircraft engines. *Chin J Aeronaut* 2013;**26**(1):9–16.
7. Eliaz N, Shachar A, Tal B, Eliezer D. Characteristics of hydrogen embrittlement, stress corrosion cracking and tempered martensite embrittlement in high-strength steels. *Eng Fail Anal* 2002;**9**(2):167–83.
8. Oehlert A, Atrens A. Stress corrosion crack propagation in AerMet100. *J Mater Sci* 1998;**33**(3):775–81.
9. Wu LF, Li SM, Liu JH, Yu M. SCC evaluation of ultra-high strength in acidic chloride solution. *J Cent South Univ* 2012;**19**(10):2726–32.
10. Liu JH, Tian S, Li SM, Yu M. Stress corrosion crack of new ultrahigh strength steel. *Acta Aeronaut Astronaut Sin* 2011;**32**(6):1164–70 Chinese.
11. Figueroa D, Robinson MJ. The effects of sacrificial coatings on hydrogen embrittlement and re-embrittlement of ultra-high strength steels. *Corros Sci* 2008;**50**(4):1066–79.

12. Figueroa D, Robinson MJ. Hydrogen transport and embitterment in 300M and AerMet100 ultra high strength steels. *Corros Sci* 2010;**52**(5):1593–602.
13. Graça MLA, Hoo CY, Silva OMM, Lourenço NJ. Failure analysis of a 300M steel pressure vessel. *Eng Fail Anal* 2009;**16**(1):182–6.
14. Ramamurthy S, Atrens A. The influence of applied stress rate on the stress corrosion cracking of 4340 and 3.5NiCrMoV steels in distilled water at 30 °C. *Corros Sci* 2010;**52**(3):1042–51.
15. Ramamurthy S, Lau WML, Atrens A. Influence of the applied stress rate on the stress corrosion cracking of 4340 and 3.5NiCrMoV steels under conditions of cathodic hydrogen charging. *Corros Sci* 2011;**53**(7):2419–29.
16. Fang BY, Han EH, Wang JQ, Ke W. Influence of strain rate on near-neutral pH environmentally assisted cracking of pipeline steels. *Acta Metall Sin* 2004;**41**(11):1174–82 Chinese.
17. Zhu LQ, Zhai JK. Electrochemical behavior in the internal corrosion cracks of 30CrMnSiNi2A. *Ordnance Mater Sci Eng* 1983;**5**(31):10–4 Chinese.
18. Zhu YC, Yang DZ. The characteristics of plastic deformation ahead of the crack tip during stress corrosion crack propagation of ultra-high strength steel 30CrMnSiNi2A and the mechanism of stress corrosion cracking. *J Beijing University Aeronaut Astronaut* 1985;**3**:139–51 [Chinese].
19. Chu WY, Li SQ, Hsiao CM, Ju SY. Effect of hydrogen on the apparent yield stress—research on the cause of hydrogen induced delayed plasticity. *Corrosion* 1981;**37**(9):514–21.
20. Chu WY. *Hydrogen damage and delayed failure*. Beijing: Metallurgical Industry Press; 1988 [Chinese].
21. Wang G, Yan Y, Li JX, Huang JY, Su YJ, Qiao LJ. Hydrogen embrittlement assessment of ultra-high strength steel 30CrMnSiNi$_2$. *Corros Sci* 2013;**77**:273–80.
22. American Society for Testing and Materials. Standard practice for slow strain rate testing to evaluate the susceptibility of metallic materials to environmentally assisted cracking. Report No.: ASTM G129-00 (2006).
23. Parkins RN. Predictive approaches to stress corrosion cracking failure. *Corros Sci* 1980;**20**(2):147–66.
24. Liu ZY, Li XG, Cheng YF. Mechanistic aspect of near-neutral pH stress corrosion cracking of pipelines under cathodic polarization. *Corros Sci* 2012;**55**:54–60.
25. Liu ZY, Li XG, Du CW, Zhai GL, Cheng YF. Stress corrosion cracking behavior of X70 pipe steel in an acidic soil environment. *Corros Sci* 2008;**50**(8):2251–7.

Liu Jianhua is a Professor at School of Materials Science and Engineering, Beihang University. He received the B.S. and M.S. degrees from Hunan University, China, and Ph.D. degree from Kobe University, Japan. His main research interests are material science and technologies, corrosion science and protection technologies, etc.

Guo Qiang is a Ph.D. candidate at school of material science and engineering, Beihang University. He received his M.S. degree from Beihang University in 2010.